NUMERICAL INVESTIGATIONS OF DYNAMIC STALL ON A ROTOR WITH CYCLIC PITCH CONTROL

Johannes Letzgus*
letzgus@iag.uni-stuttgart.de
University of Stuttgart, IAG
Stuttgart, Germany

Anthony D. Gardner
tony.gardner@dlr.de
German Aerospace Center (DLR)
Göttingen, Germany

Till Schwermer
till.schwermer@dlr.de
German Aerospace Center (DLR)
Göttingen, Germany

Manuel Keßler
kessler@iag.uni-stuttgart.de
University of Stuttgart, IAG
Stuttgart, Germany

Ewald Krämer
kraemer@iag.uni-stuttgart.de
University of Stuttgart, IAG
Stuttgart, Germany

Abstract

Numerical investigations of three-dimensional dynamic stall on a two-bladed Mach-scaled rotor ($R = 0.65\,m$, $Ma_{75} = 0.21$, $Re_{75} = 3.5 \times 10^5$) with 1/rev cyclic pitch control are presented and compared to experimental surface pressure and PIV data. In addition to URANS simulations using the finite-volume flow solvers FLOWer and TAU, a delayed detached-eddy simulation (DDES) with Menter SST as underlying RANS model is carried out with FLOWer. Facing dynamic stall and flow separation, the DDES reproduces high-frequency load fluctuations, cycle-to-cycle variations and small-scale vortical structures as seen in the experiment, which is not the case with URANS. However, common hybrid RANS-LES issues – grid-induced separation and the grey area problem – play a role in this DDES and influence loads severely. FLOWer SST simulations yield load peaks of the same magnitude as individual, non-phase-averaged measurements. With TAU SST the dynamic stall event is delayed and weakened compared to FLOWer SST and experimental results. FLOWer and TAU results using the SA turbulence model are fairly comparable but in bad agreement with the experiment at the outboard station at $r/R = 0.77$, where they exhibit no dynamic stall at all.

1 NOMENCLATURE

c	blade chord (m)
$c_l M^2$	local lift coefficient (-)
$c_m M^2$	local pitching moment coefficient (-)
$c_p M^2$	pressure coefficient (-)
f	rotational frequency (Hz)
f_d	DDES shielding function (-)
M	Mach number (-)
r	radial location (m)
R	rotor radius (m)
Re	Reynolds number (-)
ss	static stall
t	time (s)
T	oscillation period (s)
u	flow velocity (m/s)
x, y, z	chordwise, spanwise, normal direction (m)
θ	root pitch angle (°)
ν_t	kinematic eddy viscosity (m²/s)
ψ	azimuth angle (°)
75	at radial station $r/R = 0.75$
$\uparrow\downarrow$	during up- or downstroke

*Corresponding author. University of Stuttgart, Institute of Aerodynamics and Gas Dynamics (IAG), Pfaffenwaldring 21, 70569 Stuttgart.

2 INTRODUCTION

Dynamic stall (DS) is an unsteady flow phenomenon which occurs on rotor blades during high-speed forward or maneuvering flight, when asymmetrical effective inflow requires large cyclic pitch control, leading to high effective angles of attack on the retreating side of the rotor. As the angle of attack temporarily exceeds the static stall angle, vortical structures evolve on the suction side of the rotor blade, increasing the lift beyond its static maximum. Then the dynamic stall vortices convect downstream and regions of high lift are shifted past the quarter chord position, which leads to strong nose-down pitching moments. Eventually, the vortical structures are shed into the wake and flow stays massively separated for a large portion of the azimuth, introducing a strong load hysteresis. Load peaks and vibrations occurring during dynamic stall are large enough to compromise the structural integrity of the rotor blade and pitch links and, thus, limit the flight envelope of a helicopter[1].

The investigation of separated flow and dynamic stall on a rotor poses a challenge both to an experimental and to a numerical setup, since flow is highly unsteady, three-dimensional and occurring in a rotating frame of reference. While most research on this

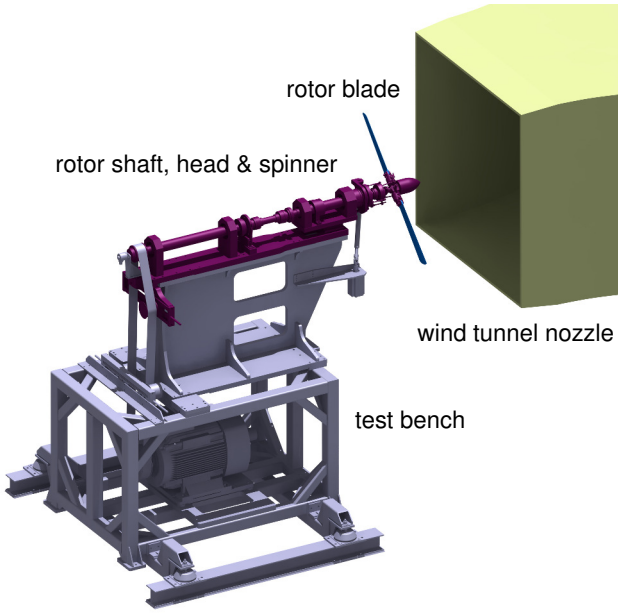

Figure 1: CAD model of the rotor test bench in front of the wind tunnel nozzle.

topic was therefore done on two-dimensional pitching airfoils or finite wings, dynamic stall is currently investigated on a two-bladed Mach-scaled rotor in the framework of a research project between the German Aerospace Center (DLR) and the Institute of Aerodynamics and Gas Dynamics (IAG) of the University of Stuttgart.

Recently, Jain et al.[2] carried out a high-resolution DDES of static and dynamic stall on an OA209 finite wing considering laminar-turbulent transition and having good agreement between the flow solvers OVERFLOW and elsA and experimental data. The grid resolutions of their setups are comparable to those investigated here, except that they did not apply a stall explicit focus region with rather cubic cells. However, their time step was half the size of the finest time step used in this study. Kaufmann et al.[3] also investigated dynamic stall on a pitching finite wing, which had the same airfoil and blade tip as the rotor blade investigated in this work. They performed URANS computations using the flow solver TAU and also considered flow transition, which improved the results regarding trailing edge flow separation. A similar setup regarding spatial resolution and grid topology is used for the TAU investigations shown here. Both investigations of dynamic stall on a finite wing achieved good results using the Menter SST turbulence model. Richez and Ortun[4] used the elsA code in URANS mode to simulate dynamic stall on an isolated rotor in forward flight considering blade deformation. They discovered three regions on the rotor disc with different stall mechanisms. One of them is rapidly growing trailing edge stall, which seems similar to the stall mechanism discovered here. Good agreement with wind tunnel test data regarding sectional loads could be achieved using a rather coarse azimuthal time-step of $\Delta\psi = 0.3\,^\circ$. Richez[5] then showed in another URANS investigation of a rotor in forward flight that dynamic stall can also be triggered by blade-vortex interaction. Again, the azimuthal time-step of $\Delta\psi = 0.3\,^\circ$ and only 5.7 million grid points per rotor blade were sufficient to capture key characteristics of dynamic stall regarding sectional loads. Very similar observations were made by Chaderjian[6] performing a SA-DDES of a UH-60A rotor. He also showed that a wake grid spacing of $10\,\%\,c_{\mathrm{tip}}$ is sufficient from an engineering point of view. The baseline FLOWer setup of this work was used in an investigation by Letzgus et al.[7] before, although with different flow conditions, carrying out a grid and time step dependency study.

3 SETUPS AND FLOW CONDITIONS

3.1 Experimental setup

The experiments were conducted in the rotor test facility (RTG) at DLR in Göttingen. The rotor axis is horizontally mounted on a test bench which is integrated into an Eiffel-type wind tunnel with a rectangular nozzle, providing a well-defined inflow. Figure 1 shows the CAD model of this setup. A swash plate is used to introduce a large cyclic pitch variation which triggers dynamic stall. The rotor radius R is 0.65 m, the rotor blade has a chord length c of 72 mm and uses a DSA-9A airfoil shape with a parabolically shaped SPP8 blade tip without anhedral. A negative twist of -9.3 $^\circ$ towards the tip is incorporated. Unsteady Kulite LQ-062 sealed gauge pressure transducers are installed in two radial cuts at $r/R = 53\,\%$ and $r/R = 77\,\%$. The pressure data is phase-averaged over 8400 dynamic stall cycles of one rotor blade. Furthermore, Particle Image Velocimetry (PIV) data at five radial stations and tuft visualizations were obtained. A more detailed overview of the RTG can be found in Schwermer et al[8]. A detailed description of the experimental setup and a comprehensive analysis of the experimental data regarding the dynamic stall case investigated in this work was presented recently by Schwermer et al.[9] as well.

3.2 Numerical setup: FLOWer

The numerical investigations conducted at IAG use the block-structured finite-volume URANS solver FLOWer[10], originally developed by DLR and considerably enhanced by IAG, utilizing a second-order implicit dual-time stepping method for time integration, the second-order spatial Jameson-Schmidt-Turkel (JST) scheme and a three-level multigrid

method. The flow is considered fully turbulent and the Menter SST as well as the Spalart-Allmaras (SA) turbulence model are used (standard formulations, no curvature/rotation corrections). In general, a hybrid RANS-LES modelling approach is believed to improve numerical investigations of separated flow, since in the LES (large-eddy simulation) region of the computational domain, the artificial eddy viscosity introduced by a turbulence model is considerably reduced and larger, energy-containing turbulent structures are resolved. Therefore – in addition to the URANS simulations – a delayed detached-eddy simulation (DDES)[11] is carried out with Menter SST as underlying RANS model[12]. Validation and first applications of DDES with the flow solver FLOWer were recently shown by Weihing[13].

On the FLOWer side, two grids are investigated. The first one, denoted *baseline* and taken from a previous investigation[7], is a typical high-resolution CH-type URANS grid. The second one, denoted *fine*, is optimized for a hybrid RANS-LES approach, as the spanwise spatial resolution is significantly increased. This is not only appropriate to resolve highly three-dimensional stalled flow, but the LES region inherently benefits from cubic cells[14]. Therefore, a dynamic stall focus region, based on results of preliminary URANS simulations, is specified, which covers the suction side of the rotor blade and the near wake with a grid size of 0.5 % c, see Figure 2. To enable this local refinement of a structured grid, there is a two-part blade grid of the CH-type: A fine near-wall grid, based on gridding guidelines of AIAA's *6th Drag Prediction Workshop*[15], covers the boundary layer. To reduce the number of grid cells, the chordwise resolution is coarsened on the lower side of the rotor blade. Also, a hanging grid-nodes interface is used to halve the spanwise resolution there. A Chimera or overset interface then connects this grid with a auto-generated Cartesian far-wall blade grid, which also uses the hanging grid-nodes technique to refine or coarsen the grid. Cell sizes and further grid data can be found in Table 1.

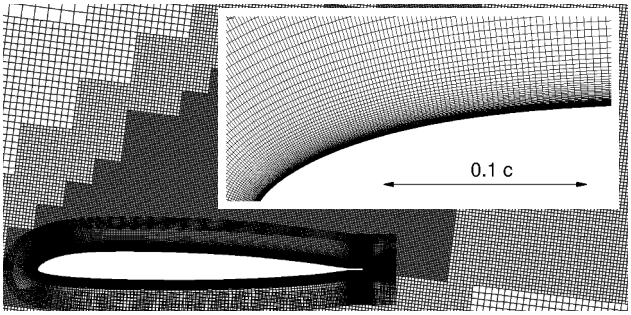

FLOWer fine

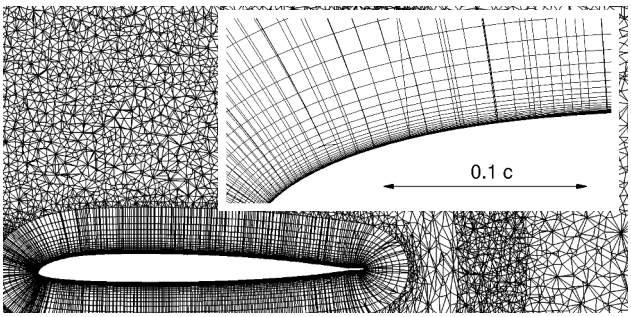

TAU

Figure 2: Spanwise slices at $r/R = 0.77$ through FLOWer fine and TAU grid and details of upper side of nose region.

The baseline as well as the fine rotor blade grid are embedded into a Cartesian background grid, which extends to a distance of 6 R (baseline) respectively 10 R (fine) from the rotor origin. To take the actual rotor hub and rotor shaft with its bearings into account, a simplified blade mount and spinner is modelled as shown in Figure 3. However, the boundary layer of the spinner is not resolved and an inviscid wall boundary condition is applied there.

Regarding the temporal resolution of simulations facing three-dimensional dynamic stall, recent investigations[16;7;5] showed that an azimuthal time-step of $\Delta\psi = 1/4\,^\circ$ (720 steps/ cycle) or even larger is sufficient to resolve key characteristics of dynamic stall. However, numerical investigations of separated flow around airfoils or finite wings[14;17;2] use much

Table 1: Cell sizes and grid data; x is in chordwise, y in spanwise and z in normal direction.

	TAU	FLOWer baseline	FLOWer fine
$\Delta x/c$ leading edge [%]	0.09	0.05	0.06
$\Delta x/c$ trailing edge [%]	0.15	0.05	0.06
$\Delta y/c$ blade tip [%]	0.11	0.90	0.08
max. $\Delta x/c$ (upper side) [%]	1.15	0.80	0.50
max. $\Delta y/c$ (upper side) [%]	3.00	6.00	0.50
Δz_1 (first cell height) [m]	3.4×10^{-6}	9.8×10^{-7}	8.0×10^{-7}
growth rate boundary layer [-]	1.25	1.15	1.10
total grid nodes [million]	31.1	56.7	238.3

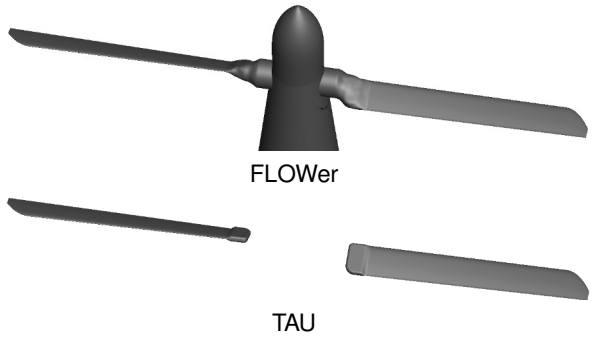

Figure 3: Modelled surfaces of the numerical setups: FLOWer with rotor blades, simplified blade mount, spinner and shaft, TAU with isolated rotor blades.

smaller time steps – especially if a DES is carried out – in the order of $\Delta t = \Delta_0 / U_{max}$, with Δ_0 being the smallest grid size and U_{max} the largest flow velocity in the respective region. Today, this is computationally not feasible for rotor applications, since many revolutions must be simulated for the flow to reach a quasi-periodic state. However, preliminary investigations showed that an azimuthal time-step of $\Delta\psi = 1/12\,^\circ$ (4320 steps/ revolution) for the baseline setup and $\Delta\psi = 1/24\,^\circ$ (8640 steps/ revolution) for the fine setup is in fact necessary to suppress numerical instabilities in form of high-frequency surface pressure fluctuations in the region of leading edge flow separation. The dual-time stepping scheme uses 20 to 65 inner iterations, which reduce the residuals at least by an order of magnitude.

3.3 Numerical setup: TAU

Additional computations are conducted at DLR Göttingen with DLR's second-order finite-volume URANS solver TAU[18], which uses unstructured hybrid grids, an implicit backward Euler and four-level multigrid method. Again, both the Menter SST and SA turbulence model are used (standard formulations, no curvature/rotation corrections) and flow is considered fully turbulent. While the boundary layer region uses prism layers, tetrahedral cells are added to the surrounding region, which extends to roughly 920 R, see Figure 2. The grid points are distributed according to Kaufmann et al[19]. Further grid information is listed in Table 1 as well. The pitching motion is resolved with 1800 azimuthal time steps per period. As Figure 3 shows, the TAU setup only models the surface of the two rotor blades. Both the FLOWer and TAU setup use rigid rotor blades, so no deformation is considered.

3.4 Flow conditions

The rotor is operated at a rotational frequency of $f_{\text{rotor}} = 23.6\,\text{Hz}$, leading to a Mach number of 0.21 and a Reynolds number of 3.5×10^5 at 75 % rotor radius. The sinusoidal variation of the root pitch angle is $\theta(t) = 23.8\,^\circ - 6.2\,^\circ \cos(2\pi\, f_{\text{rotor}}\, t)$, which triggers dynamic stall. The experiments were carried out with a wind tunnel exit velocity of 2.2 m/s. To take this into account, the numerical investigations use a uniform axial inflow velocity of the same magnitude.

4 RESULTS

4.1 Static hover case

To gain confidence in the numerical setups, a hover test case with 24 ° static root pitch angle is investigated at first. This root pitch angle is about 2.7 ° below the static stall angle and leads to a highly loaded rotor with fully attached flow. The pressure distributions in Figure 4 exhibit on the one hand an overall good agreement between computations and experiment and on the other hand very good agreement between FLOWer and TAU. Both computations yield slightly higher lift at the leading part of the suction side, where laminar-turbulent transition occurs in the experiment[9]. The measured integral rotor thrust in this case is 150.4 N compared to 150.9 N (+0.3 %) computed by FLOWer. Interestingly enough, the pressure distributions at $r/R = 0.31$ also agree well between both computations, although the modelled geometries strongly differ at the blade root, which begins at $r/R = 0.25$. The good numerical results of this static hover case give reasons to believe that influences of blade elasticity, test bench, rotor head and shear layer of the wind tunnel jet only play a negligible role here.

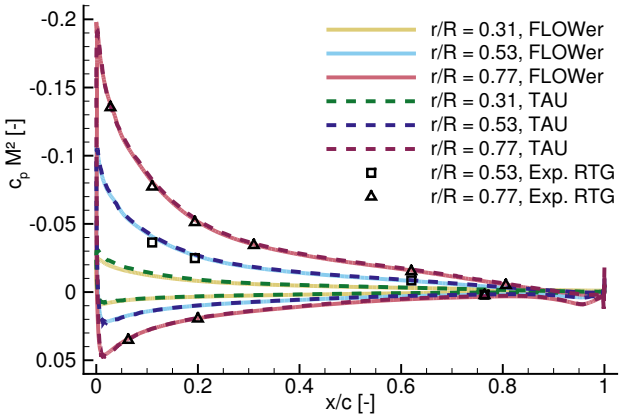

Figure 4: Pressure distributions of CFD and experiment for a highly loaded hover case with a static root pitch angle of $\theta = 24\,^\circ$.

4.2 Dynamic stall case

4.2.1 FLOWer URANS and DDES investigations

A key aspect of dynamic stall is the overshoot of lift and nose-down pitching moment. Here, the local load coefficients at the radial station $r/R = 0.77$, where nine pressure sensors are available in the experiment, are compared. Consequently, the numerical coefficients are integrated from surface pressure taken only at the experimental pressure-tap positions (see Figure 9) as well. Schwermer et al.[9] showed that this is reasonable and yields qualitatively similar polars.

In Figure 5, FLOWer load coefficients are compared to those of the experiment. The error bars represent the standard deviation of the phase-averaged experimental data. First, it shows that the URANS results using the baseline and the fine grid are very similar during the whole upstroke and minor differences are only found during the downstroke, when the polars exhibit a strong hysteresis due to complete flow separation. Secondly, URANS and DDES load coefficients are the same during most part of the upstroke until $\theta \approx 27\,°\uparrow$. During this linear phase, FLOWer yields a slightly higher lift and pitching moment than the experiment, especially at the lower turning point of the cycle. Continuing the upstroke until $\theta \approx 29\,°\uparrow$, lift of DDES and experiment stops rising, while the slope of the URANS solutions' lift remains constant. Then, with DDES, a strong peak in additional lift and (negative) nose-down pitching moment occurs more than 0.5 ° earlier than in the experiment or with URANS, which stalls last. Just before the upper turning point, the pitching moment rises to a pre-stall level and then drops rapidly again, as the blade starts to pitch down. During the downstroke, lift hysteresis of DDES is strongest and URANS agrees better with the experiment. Regarding the pitching moment, the URANS solutions show a somewhat earlier recovery.

Here, the computational maximum of lift and pitching moment exceeds the phase-averaged maximum of the experiment significantly and occurs as a distinct peak. However, it is known that phase-averaging of experimental pressure data to some extent cancels out peak values, as stall onset and aerodynamic peak values change from cycle to cycle[20;3]. Therefore, non-phase-averaged load coefficients of four consecutive, arbitrarily chosen, dynamic stall cycles are plotted in Figure 6 and it becomes apparent that the experimental lift as well as the pitching moment reach peak values comparable to those of the computations. It also shows that there is almost no cycle-to-cycle variation with URANS, even during the downstroke, when flow is massively separated. In contrast, DDES yields high-frequency fluctuations and cycle-to-cycle variations comparable to those of the experiment.

Judging only from Figure 5 and 6, the characteristic dynamic stall event, that is a sudden peak in nose-down pitching moment and lift overshoot triggered by leading-edge flow separation with vortex formation and convection, seems to simply occur earlier in the cycle of the DDES. Facing premature separation in combination with a hybrid RANS-LES approach, the well-known issue of modelled stress depletion (MSD) causing grid-induced separation (GIS)[21;11] comes to mind. Here, the LES region intrudes too far into the boundary layer, which reduces the Reynolds stresses and consequently the modelled transfer of momentum. A cut through the boundary layer at $r/R = 0.77$ and $x/c = 0.75$ at an early point during the upstroke shows that with DDES, the eddy viscosity ν_t is in fact reduced in the outer part of the boundary layer,

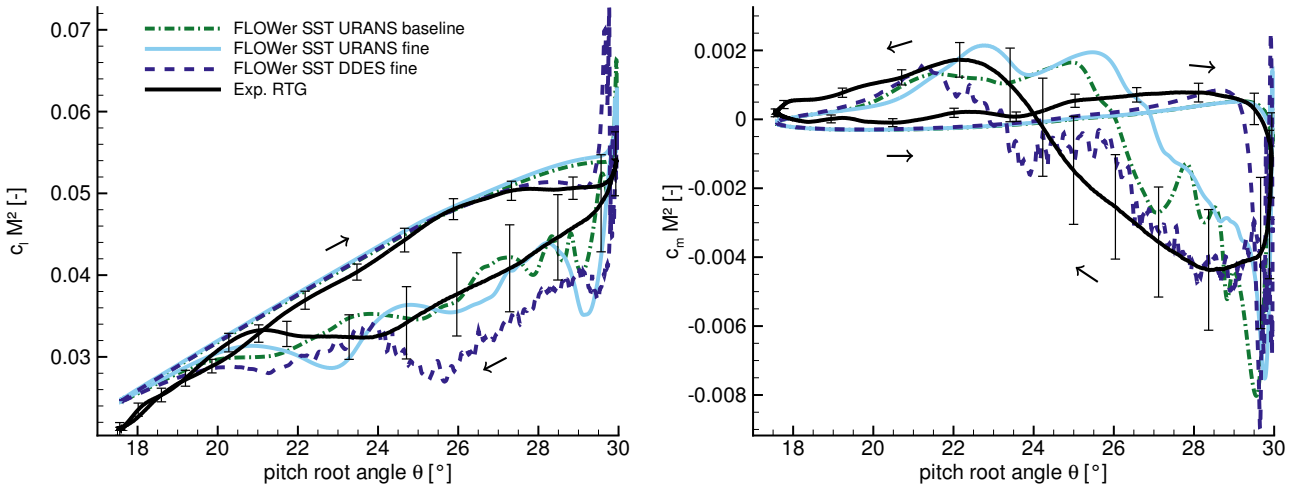

Figure 5: Comparison of experimental (phase-averaged) and numerical (reduced data, phase-averaged over four dynamic stall cycles) local lift and pitching moment coefficients at $r/R = 0.77$. The numerical data is from FLOWer URANS baseline/ fine and FLOWer DDES fine simulations.

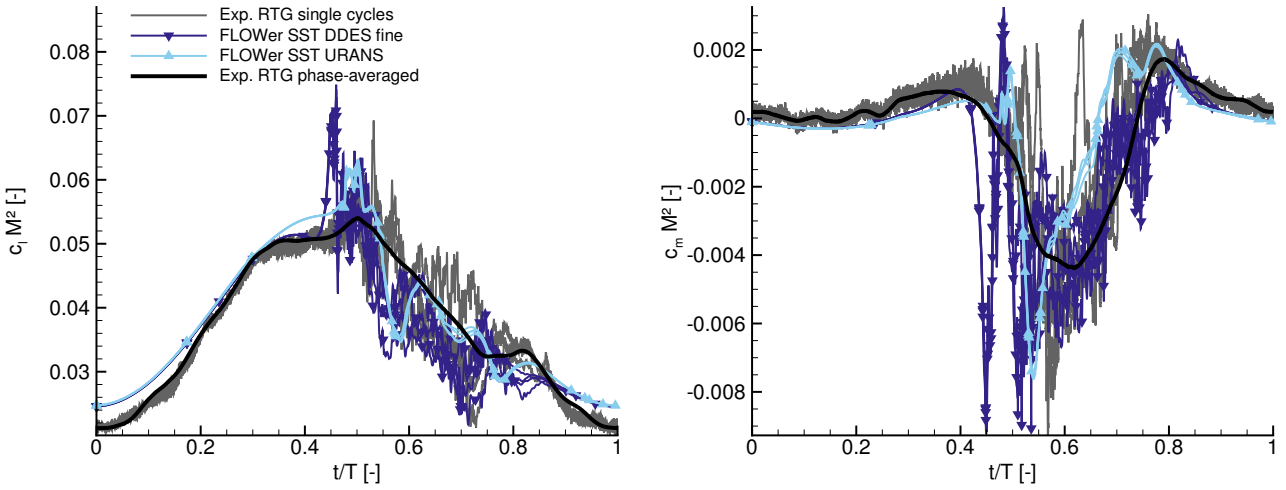

Figure 6: Comparison of non-phase-averaged experimental and numerical (reduced data) lift and pitching moment coefficients at $r/R = 0.77$ of four consecutive dynamic stall cycles.

where the shielding function $1 - f_d$ drops from one to zero, see Figure 7. While in theory[11], $1 - f_d$ should not drop to zero until the edge of the boundary layer, the LES mode in this case is activated at half of the boundary layer height. Recently, similar observations with high-resolution DDES facing adverse pressure gradients were made by others[22;23;24;25], who also proposed some recalibrations of the model. In summary, it cannot be completely ruled out that grid-induced separation occurs in this DDES, although the flattening of the lift polar around $\theta = 27\,^\circ\uparrow$ agrees well with the experiment.

Figure 8, showing surface streamlines on the suction side, reveals that with DDES, the upstream and outboard extent of trailing edge flow separation is larger than with URANS at earlier stages of the cycle ($t/T = 0.37, 0.40$). Likewise, instantaneous in-plane streamlines at $r/R = 0.77$ indicate a distinct region of flow recirculation above the trailing edge only with DDES, see $t/T = 0.40$ in Figure 10. The growing trailing edge flow separation observed in all simulations resembles Leishman's[1] definition of the first stage of dynamic stall.

Moving on in time to $t/T = 0.45$, the DDES surface solution exhibits very low pressure around mid-chord between $0.55 < r/R < 0.83$. This bar-shaped region looks somewhat similar to the footprint of a dynamic stall vortex of a URANS simulation, and indeed, the recirculation zone evolving at the trailing edge has grown and moved upstream, forming a strong vortex at $x/c \approx 0.6$, which induces massive flow reversal (Figure 10). It is worth noting that this vortex evolves from the free shear layer at a fixed chordwise position and must not be confused with a dynamic stall vortex convecting from the leading edge. Quite the contrary, the beginning of a dynamic stall event can be seen just downstream the leading

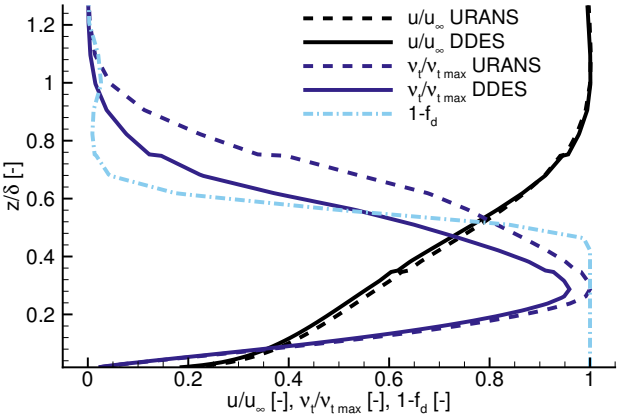

Figure 7: Boundary layer data of FLOWer fine URANS and DDES at $x/c = 0.75$, $r/R = 0.77$ and $t/T = 0.3$ (upstroke).

edge between $0.55 < r/R < 0.75$. This becomes more obvious in Figure 9, where near-leading-edge low pressure peaks in the pressure distributions indicate dynamic stall. Thus, the earlier peaks of nose-down pitching moment and lift observed in the DDES load polars are the result of short-term low pressure around mid-chord, which is neither present in the experiments nor in the URANS simulations. It is believed that this is related to another major issue of every hybrid RANS-LES approach, the so called grey area problem[26]. In this case, the free shear layer stays stable for too long, since the LES region is, of course, not fed with resolved turbulent structures from the RANS region. In addition, it lacks the ability to resolve initial small shear layer instabilities, on the one hand due to insufficient grid resolution and on the other hand due to damping effects of the close-by RANS region[27]. Thus, the free shear layer breakup is non-physically delayed, which might allow the mentioned non-dynamic stall vortex to roll up and to gain

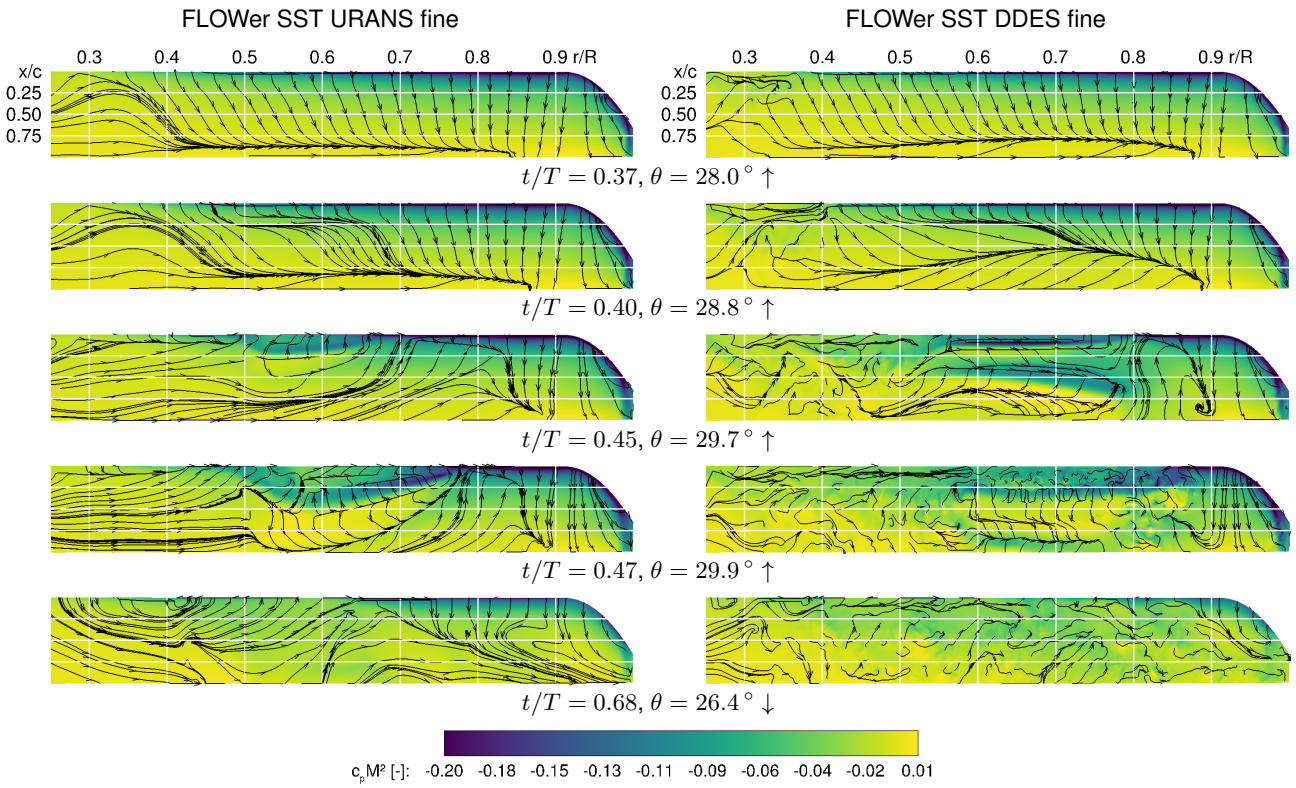

Figure 8: Comparison of instantaneous distributions of surface pressure and surface streamlines on the suction side between FLOWer URANS and DDES at several points during one cycle of dynamic stall.

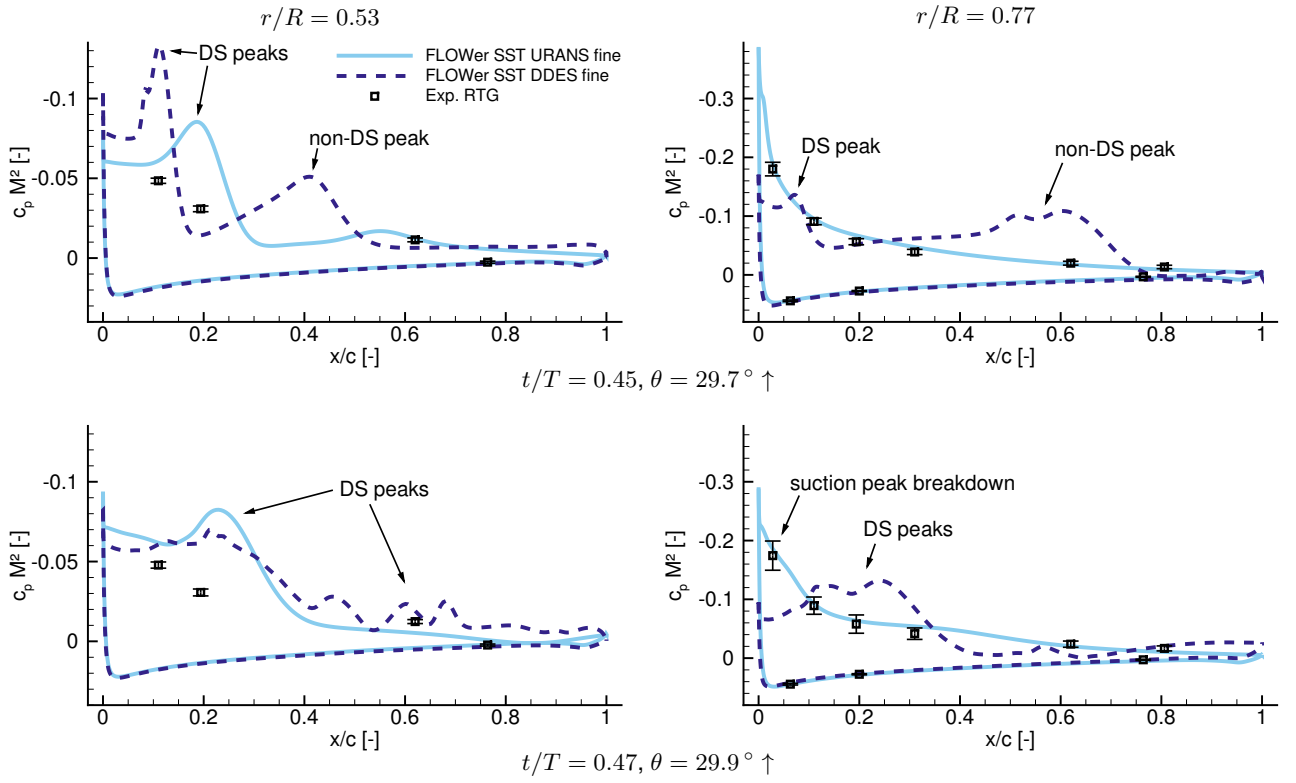

Figure 9: Pressure distributions comparing experiment (phase-averaged) and FLOWer fine URANS and DDES results (single phase) at several points during one cycle of dynamic stall.

such strength. According to high-fidelity LES investigations[28] and PIV measurements[29] of dynamic stall onset on oscillating airfoils the free shear layer should quickly develop downstream convecting, small-scale vortical structures due to the Kelvin-Helmholtz instability.

Still at $t/T = 0.45$, both the surface solution and the pressure distribution of the URANS simulation already indicate dynamic stall more inboard, between $0.5 < r/R < 0.65$. In the experiment, the pressure distribution implies a conventional suction peak and the low standard deviation in phase-averaged pressures suggest that this is not the case (Figure 9).

A moment later at $t/T = 0.47$, the free shear layer of DDES finally breaks up into smaller, incoherent vortical structures which quickly convect downstream, while at the leading edge, several dynamic stall vortices become visible. The URANS dynamic stall vortex is rather compact and stays close to the surface. Basically no disturbance of the flow can yet be seen in the instantaneous PIV image, see Figure 10 again. As the URANS surface solution shows, the omega-shaped vortex grows in- and outboard and is about to reach $r/R = 0.77$. At this point, the URANS pressure distribution matches the experiment's very well. Both the deformed URANS suction peak and the significantly increased standard deviation of the experimental pressure sensor at $x/c = 0.03$ indicate the beginning of leading edge stall. The connection between stall and rising standard deviation of pressure sensors is described e.g. by Gardner[30]. However, at the inner radial station at $r/R = 0.53$, there is still

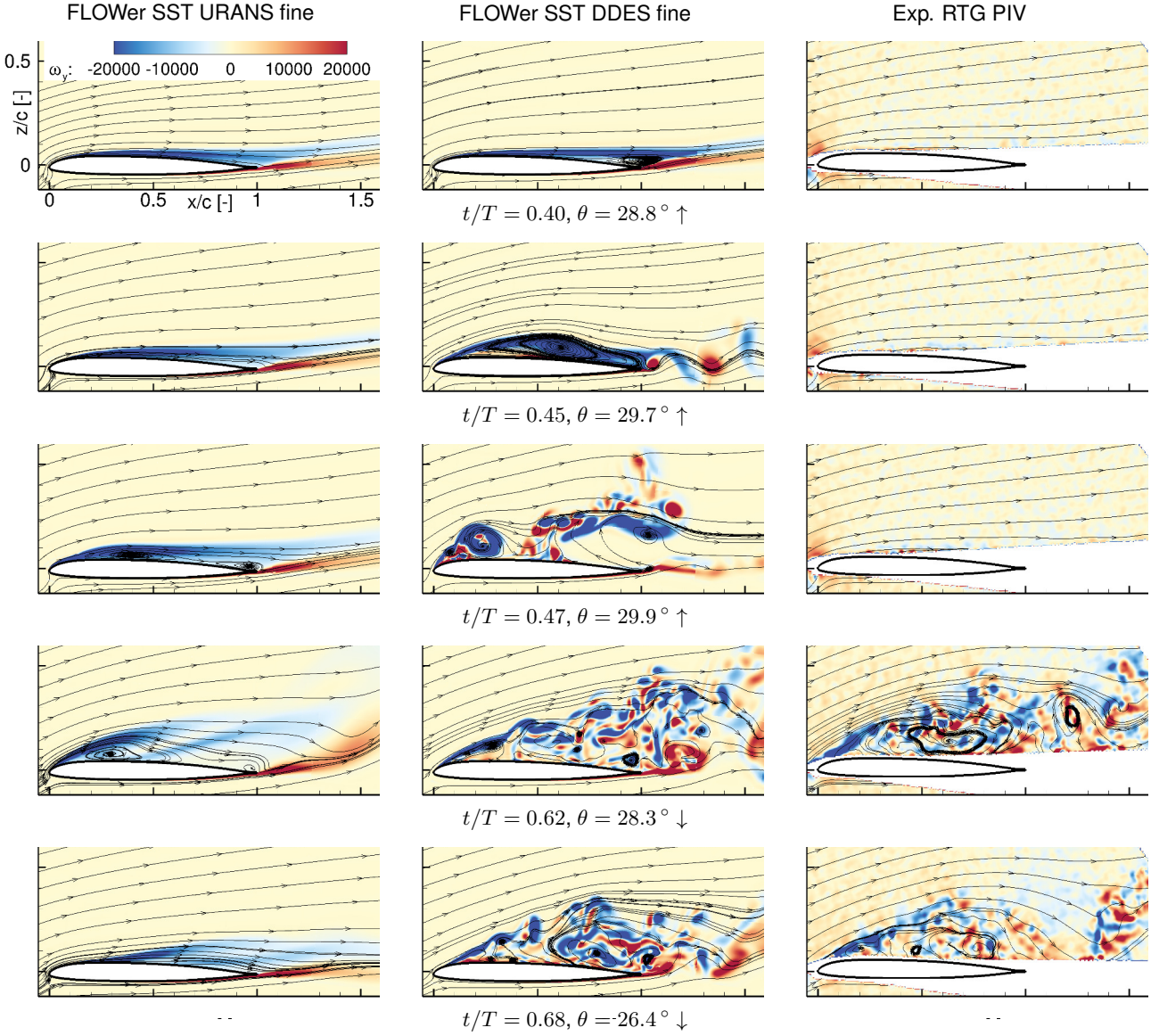

Figure 10: Comparison of contours of instantaneous in-plane vorticity and in-plane streamlines at $r/R = 0.77$ between FLOWer computations and experiment at several points during one cycle of dynamic stall.

no sign of dynamic stall in the experiment. Comparing the pressure distributions of the simulations, it is also apparent that the shedding of dynamic stall vortices happens earlier in the cycle of DDES, as the low pressure peaks are already convected further downstream.

As soon as there is complete leading edge flow separation, for instance at at $t/T = 0.62$, DDES works as expected and is able to capture the flow field at $r/R = 0.77$ very well: The instantaneous vorticity contours indicate turbulent structures, which are as incoherent and chaotic as in the experiment. Also, the size and shape of structures and vertical extent of the separated flow matches well. In contrast, URANS computations exhibit a coherent recirculation zone and the extent of flow separation is already declining.

Finally at $t/T = 0.68$, both the surface solutions and the in-plane flow field at $r/R = 0.77$ of the URANS simulation exhibit flow reattachment starting at the leading edge of the outboard region. Flow remains disturbed only close to the surface and at the rear of the rotor blade, where it has a strong tip-wise directed component. With DDES, flow is still massively separated, indicated by rather chaotic surface streamlines. The dividing in-plane streamline of the DDES (Figure 10) is similar to the one of the experiment and covers a region of flow separation with a vertical extent of still one third of the chord length. Again, the vortical structures of the DDES are quite comparable to those obtained from PIV data.

4.2.2 Comparison of FLOWer and TAU URANS investigations

During most part of the upstroke, when the root pitch angle is below it's static stall angle ($\theta_{ss} \approx 26.7\,°$) and flow is fully attached, all simulations are expected to yield very similar results. Regarding local lift and pitching moment coefficients at $r/R = 0.77$, Figure 11 confirms that this is the case. Then, between θ_{ss} and the upper turning point, all URANS simulations fail to capture the flattening of the experimental lift polar, and both TAU solutions yield slightly higher lift than FLOWer. At the upper turning point, neither both TAU simulations nor FLOWer SA show an additional sharp lift peak observed in the experiment and with FLOWer SST. Those three simulations also do not have any moment stall there. At around $\theta = 28\,° \downarrow (t/T = 0.63)$ of the downstroke, the TAU SST solution exhibits a steep but short rise in nose-down pitching moment, which indicates a delayed and weakened dynamic stall event. In general, both simulations using the SA turbulence model yield fairly similar pitching moments throughout the whole cycle, have weaker lift hysteresis and show no clear signs of dynamic stall at this radial station.

The pressure distributions in Figure 12 reveal that at the upper turning point ($t/T = 0.50$), both TAU simulations and FLOWer SA retain a substantial suction peak. At the inner radial station at $r/R = 0.53$ this seems to agree well with the experiment considering the low standard deviation, outboard at $r/R = 0.77$ it does not. Moving on in time to $t/T = 0.52$ the surface pressure barely changes at $r/R = 0.77$, but at $r/R = 0.53$ both TAU solutions show a breakdown of the leading edge suction peak and the downstream convection of a low pressure peak, lagging behind the FLOWer SST solution. Finally at $t/T = 0.65$ TAU SST is also mostly stalled at $r/R = 0.77$ and low pressure is shifted downstream the quarter chord point, inducing the nose-down pitching moment peak seen in the local polar, while both SA solutions keep their strong suction peak. At the inner station at $r/R = 0.53$, only the FLOWer SA solution shows no dynamic stall event

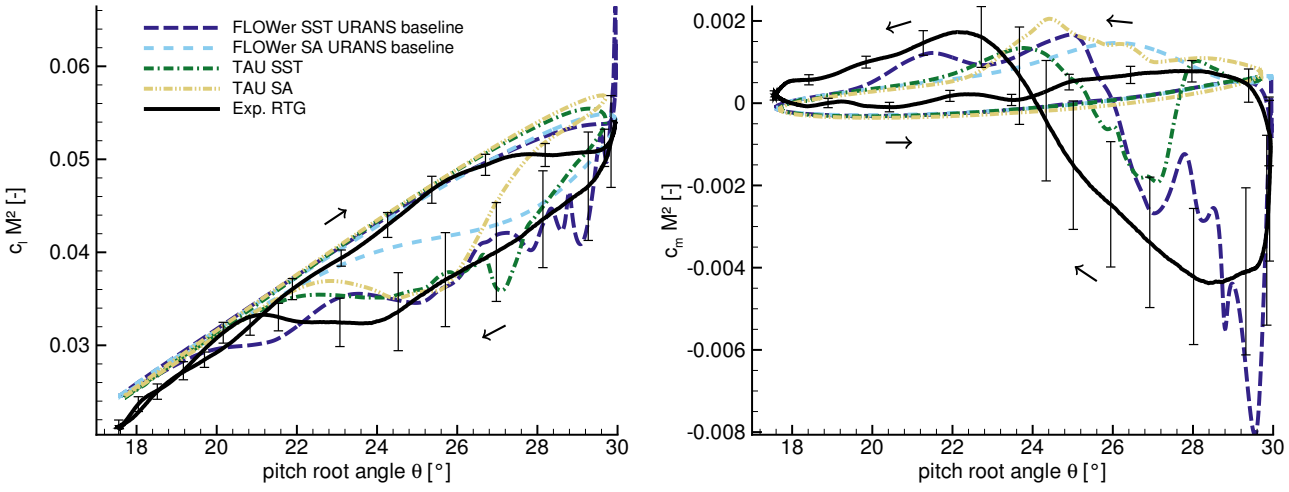

Figure 11: Comparison of experimental (phase-averaged) and numerical (reduced data, single cycle) local lift and pitching moment coefficients at $r/R = 0.77$. The numerical data is from FLOWer baseline and TAU simulations (URANS).

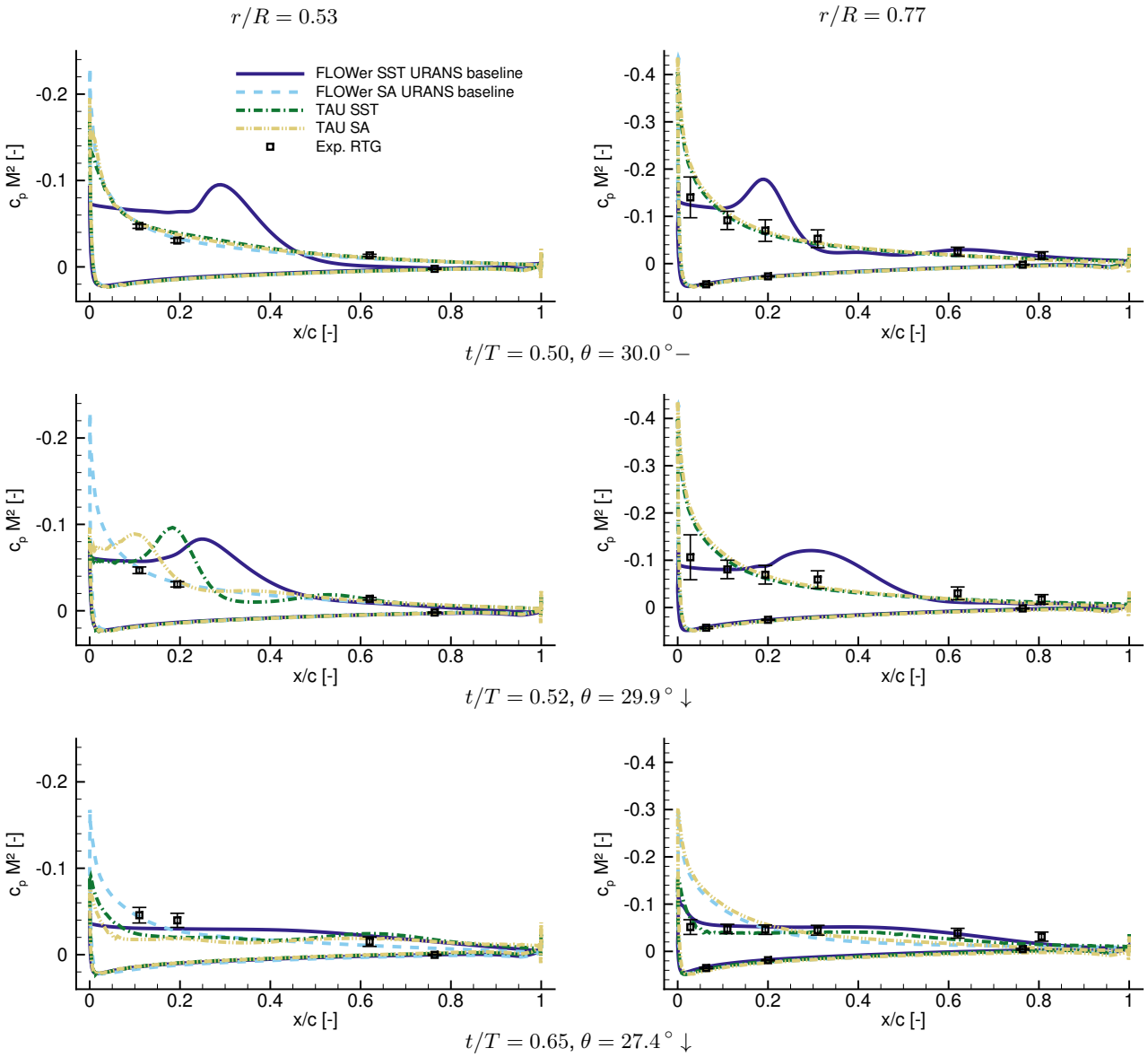

Figure 12: Pressure distributions comparing FLOWer baseline and TAU simulations (single phase) and experiment (phase-averaged) at several points during one cycle of dynamic stall.

throughout the complete cycle. Regarding the experiment, the increased standard deviation of the two pressure sensors at $x/c = 0.11$ and $x/c = 0.19$ suggests that there finally is flow separation at the leading part of the suction side.

Comparing pressure distributions and surface streamlines of TAU SST in Figure 13 with those of FLOWer SST URANS in Figure 8 during the upstroke at $t/T = 0.37$, small differences are only found in the innermost region of the blade. This is most likely due to the different blade mount treatment, which permits flow around the blade root and formation of a root vortex in case of the TAU setup. At $t/T = 0.40$ there still is only weak trailing edge separation with TAU, while FLOWer already shows a second separation line around the quarter chord line and strong spanwise flow inboard of $r/R \approx 0.7$. With TAU, a typical omega-shaped footprint of a dynamic stall vortex can then be seen during the downstroke at $t/T = 0.55$. Compared with FLOWer, where such an event is seen much earlier at $t/T = 0.47$, induced pressure is not as low and the footprint is more inboard. Since the dynamic stall event of TAU is delayed beyond the upper turning point of the pitching motion, it seems plausible that the vortical structure itself has a different strength and spread. Finally at $t/T = 0.68$ flow reattachment is already more advanced with TAU, especially in the blade tip region.

Figure 14 visualizes main dynamic stall vortices of all simulations which use the SST turbulence model. Since it was found that the dynamic stall events do not happen simultaneously, different points in time are

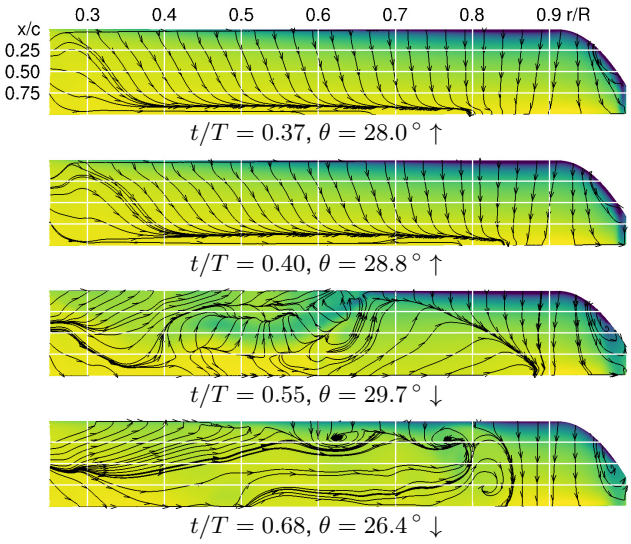

Figure 13: Instantaneous distributions of surface pressure and surface streamlines on the suction side of the TAU SST URANS simulation at several points during one cycle of dynamic stall (contours legend see Figure 8).

chosen. DDES has mostly small-scale, incoherent vortical structures, except in the wake, where tube-shaped structures indicate typical URANS flow separation resembling a Kármán vortex street. They evolved early in the cycle, when the LES mode was either not yet active or failed to simulate the decay of large-scale vortical structures. DDES also exhibits smaller, secondary vortex filaments orbiting the main blade tip vortex. As assumed before, the dynamic stall vortex of FLOWer URANS convects more outboard and is more distinct than the one of TAU. The broad sheet of λ_2-structures in the wake of the TAU solution might be related to the unstructured grid.

5 CONCLUSIONS

In this work numerical investigations of three-dimensional dynamic stall on a two-bladed Mach-scaled rotor with 1/rev cyclic pitch control were carried out and compared to experimental surface pressure and PIV data. In addition to URANS simulations using the finite-volume flow solvers FLOWer (structured) and TAU (hybrid unstructured), a high-resolution delayed detached-eddy simulation (DDES) with Menter SST as underlying RANS model was performed using FLOWer. The URANS simulations were carried out with both the Menter SST and SA turbulence model. In all simulations the flow was considered fully turbulent at all times. The main findings are as follows:

- Good agreement between experimental results, FLOWer and TAU simulations of a static, highly loaded hover case has been achieved. Influences of blade elasticity, rotor head and test bench components as well as shear layer effects of the wind tunnel jet seem to be negligible.

- In case of dynamic stall, only the DDES captures the flattening of the lift polar beyond the static stall angle seen in the experiment. It is also able to reproduce physically realistic high-frequency load fluctuations and cycle-to-cycle variations if flow is separated, which is not possible with URANS. In case of complete flow separation, only the DDES flow field agrees well with PIV data regarding size and shape of incoherent vortical structures and form of dividing streamlines.

- The main issues of a hybrid RANS-LES approach – modelled stress depletion (MSD) causing grid-induced separation (GIS) and the grey area problem – are likely to exist both in this DDES case. During the complex transition from attached to completely separated flow, the latter seems to support the formation of a strong vortex from the free shear layer, which severely influences lift and nose-down pitching moment and is not seen in URANS and experimental results.

- For the most part of the upstroke, as long as flow is attached, all simulations yield the same local loads at $r/R = 0.77$, which match the experimental loads fairly well. Load peaks of the FLOWer SST simulations are of the same magnitude as of non-phase-averaged measurements. However, phase-averaging of experimental data reduces peak values significantly.

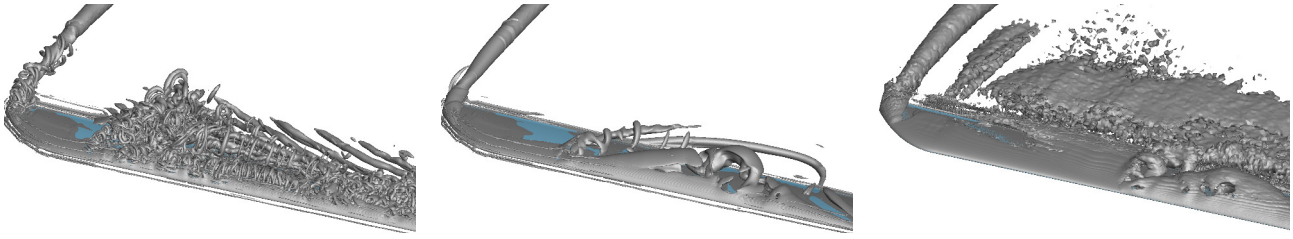

FLOWer SST DDES fine, $t/T = 0.47$ FLOWer SST URANS fine, $t/T = 0.50$ TAU SST URANS, $t/T = 0.55$

Figure 14: Visualization of dynamic stall vortices by means of instantaneous isosurfaces of the λ_2-criterion.

- With TAU SST, dynamic stall occurs delayed and much weaker than with FLOWer SST. As one single reason for that could not be found, a combination of differences in grids and implementation and usage of numerical schemes is assumed to be the issue. The SA solutions of FLOWer and TAU agree better and show the same non-stall behaviour outboard at $r/R = 0.77$. Consequently, they completely fail to capture dynamic stall there. More inboard at $r/R = 0.53$ TAU SA shows only weak dynamic stall while FLOWer SA shows no leading edge stall throughout the complete cycle.

ACKNOWLEDGEMENTS

This work was funded by DFG grant *Untersuchung der dreidimensionalen dynamischen Strömungsablösung an Rotorblättern* (Investigation of three-dimensional dynamic stall on rotor blades) and the DLR project *FAST-Rescue*. Computing resources have been provided by the High Performance Computing Centre Stuttgart under project *HELISIM* and the Leibniz Supercomputing Centre under grant *pr83su*.

REFERENCES

[1] J. Gordon Leishman. *Principles of Helicopter Aerodynamics*. Cambridge University Press, 2nd edition, 2006.

[2] Rohit Jain, Arnaud Le Pape, Michel Costes, François Richez, and Marilyn Smith. High-resolution CFD predictions for static and dynamic stall of a finite-span OA209 wing. In *Proceedings of the 72nd Annual Forum of the American Helicopter Society*, 2016.

[3] Kurt Kaufmann, Christoph B. Merz, and Anthony D. Gardner. Dynamic stall simulations on a pitching finite wing. *Journal of Aircraft*, 2017.

[4] François Richez and Biel Ortun. Numerical investigation of the flow separation on a helicopter rotor in dynamic stall configuration. In *Proceedings of the 42nd European Rotorcraft Forum*, 2016.

[5] François Richez. Numerical analysis of dynamic stall for different helicopter rotor flight conditions. In *Proceedings of the 73rd Annual Forum of the American Helicopter Society*, 2017.

[6] Neal M. Chaderjian. Navier-Stokes simulation of UH-60A rotor/wake interaction using adaptive mesh refinement. In *Proceedings of the 73rd Annual Forum of the American Helicopter Society*, 2017.

[7] Johannes Letzgus, Manuel Keßler, and Ewald Krämer. CFD-simulation of three-dimensional dynamic stall on a rotor with cyclic pitch control. In *Proceedings of the 41th European Rotorcraft Forum*, 2015.

[8] Till Schwermer, Kai Richter, and Markus Raffel. Development of a rotor test facility for the investigation of dynamic stall. In *New Results in Numerical and Experimental Fluid Mechanics X*, pages 663–673. Springer, 2016.

[9] Till Schwermer, Anthony D. Gardner, and Markus Raffel. Dynamic stall experiments on a rotor with high cyclic setting in axial inflow. In *Proceedings of the 73rd Annual Forum of the American Helicopter Society*, 2017.

[10] Jochen Raddatz and Jens K. Fassbender. Block structured Navier-Stokes solver FLOWer. In *MEGAFLOW-Numerical Flow Simulation for Aircraft Design*, pages 27–44. Springer, 2005.

[11] Philippe R. Spalart, Sébastien Deck, Michael L. Shur, Kyle D. Squires, Michael Kh. Strelets, and Andrei Travin. A new version of Detached-Eddy Simulation, resistant to ambiguous grid densities. *Theoretical and computational fluid dynamics*, 20(3):181–195, 2006.

[12] Mikhail S. Gritskevich, Andrey V. Garbaruk, and Florian R. Menter. Fine-tuning of DDES and IDDES formulations to the k-ω shear stress transport model. In *Progress in Flight Physics*, volume 5, pages 23–42. EDP Sciences, 2013.

[13] Pascal Weihing, Johannes Letzgus, Galih Bangga, Thorsten Lutz, and Ewald Krämer. Hybrid RANS/LES capabilities of the flow solver FLOWer - application to flow around wind turbines. In *Proceedings of the 6th Symposium on Hybrid RANS-LES Methods*, 2016.

[14] Philippe R. Spalart. Young-person's guide to Detached-Eddy Simulation grids, 2001.

[15] American Institute of Aeronautics and Astronautics (AIAA). 6th Drag Prediction Workshop. Gridding guidelines. `https://aiaa-dpw.larc.nasa.gov/Workshop6/DPW6_gridding_guidelines_2015-08-28.pdf`, 2015. [Online; accessed 31-May-2017].

[16] Reza Nilifard, Alex Zanotti, Giuseppe Gibertini, Alberto Guardone, and Giuseppe Quaranta. Numerical investigation of three-dimensional effects on deep dynamic stall experiments. In *Proceedings of the 71st Annual Forum of the American Helicopter Society*, 2015.

[17] François Richez, Arnaud Le Pape, and Michel Costes. Zonal Detached-Eddy Simulation of separated flow around a finite-span wing. *AIAA Journal*, 53(11):3157–3166, 2015.

[18] Dieter Schwamborn, Anthony D. Gardner, Heiko von Geyr, Andreas Krumbein, Heinrich Lüdeke, and Arne Stürmer. Development of the DLR TAU-code for aerospace applications. In *Proceedings of the International Conference on Aerospace Science and Technology*, pages 26–28. National Aerospace Laboratories Bangalore, India, 2008.

[19] Kurt Kaufmann, Michel Costes, François Richez, Anthony D. Gardner, and Arnaud Le Pape. Numerical investigation of three-dimensional static and dynamic stall on a finite wing. *Journal of the American Helicopter Society*, 60 (3), 2015.

[20] Manikandan Ramasamy, Jacob S. Wilson, William J. McCroskey, and Preston B. Martin. Measured characteristics of cycle-to-cycle variations in dynamic stall. In *Proceedings of the American Helicopter Society Technical Meeting on Aeromechanics Design for Vertical Lift*, pages 1–34, 2016.

[21] Florian R. Menter, Martin Kuntz, and Robin Langtry. Ten years of industrial experience with the SST turbulence model. *Turbulence, heat and mass transfer*, 4(1):625–632, 2003.

[22] Axel Probst, Rolf Radespiel, Christoph Wolf, Tobias Knopp, and Dieter Schwamborn. A comparison of Detached-Eddy Simulation and Reynolds-stress modelling applied to the flow over a backward-facing step and an airfoil at stall. In *Proceedings of the 48th AIAA Aerospace Sciences Meeting Including the New Horizons Forum and Aerospace Exposition*, pages 2010–0920, 2010.

[23] Neil Ashton. Recalibrating Detached-Eddy Simulation to eliminate modelled-stress depletion. In *Proceedings of the 23rd AIAA Computational Fluid Dynamics Conference*, 2017.

[24] Nishan Jain, Bumseok Lee, and James D. Baeder. Assessment of shielding parameters in conventional DDES method under the presence of alternative turbulence length scales. In *Proceedings of the 23rd AIAA Computational Fluid Dynamics Conference*, 2017.

[25] Veer N. Vatsa, David P. Lockard, and Philippe R. Spalart. Grid sensitivity of SA-based Delayed-Detached-Eddy-Simulation model for blunt-body flows. *AIAA Journal*, 2017.

[26] Philippe R. Spalart, WH Jou, Michael Strelets, and Steven R. Allmaras. Comments on the feasibility of LES for wings, and on a hybrid RANS/LES approach. *Advances in DNS/LES*, 1:4–8, 1997.

[27] Charles Mockett. *A Comprehensive Study of Detached-Eddy Simulation*. Universitätsverlag TU Berlin, 2009.

[28] Miguel R. Visbal. Analysis of the onset of dynamic stall using high-fidelity Large-Eddy Simulations. In *Proceedings of the 52nd AIAA Aerospace Sciences Meeting*, 2014.

[29] Karen Mulleners and Markus Raffel. Dynamic stall development. *Experiments in Fluids*, 54(2):1469, 2013.

[30] Anthony D. Gardner, Christian C. Wolf, and Markus Raffel. A new method of dynamic and static stall detection using infrared thermography. *Experiments in Fluids*, 57(9):149, 2016.